Int J Mech Mater Des (2018) 14:177–193
https://doi.org/10.1007/s10999-017-9370-9

Numerical modeling of strain localization in engineering ductile materials combining cohesive models and X-FEM

J. Wolf · P. Longère · J. M. Cadou · J. P. Crété

Received: 30 March 2017 / Accepted: 5 April 2017 / Published online: 11 April 2017

Abstract The present work aims at numerically predicting the current residual strength of large engineering structures made of ductile metals against accidental failure. With this aim in view, the challenge consists in reproducing within a unified finite element-based methodology the successive steps of micro-voiding-induced damage, strain localization and crack propagation, if any. A key ingredient for a predictive ductile fracture model is the proper numerical treatment of the critical transition phase of damage-induced strain localization inside a narrow band. For this purpose, the strong discontinuity cohesive model and the eXtended Finite Element Method are combined. A propagation algorithm is proposed and studied in the context of ductile materials. Physics-motivated criteria to pass from the phase of more or less diffuse damage to strain localization and from strain localization to crack propoagation are proposed. Finally, a 2D numerical example is shown to study the performance of the failure analysis model when implemented into an engineering finite element computation code, namely Abaqus.

Keywords Ductile failure · Strain localization · EXtended Finite Element Method · Cohesive band model

J. Wolf · P. Longère (✉)
Université de Toulouse, ISAE-SUPAERO, Institut Clément Ader (CNRS 5312), 3 rue Caroline Aigle, 31400 Toulouse, France
e-mail: patrice.longere@isae.fr

J. M. Cadou
Université Européenne de Bretagne, UBS, Institut de Recherche Dupuy de Lôme (CNRS 3744), Rue Saint Maudé, 56100 Lorient, France

J. P. Crété
Institut Polytechnique Grand Paris, SUPMECA, QUARTZ (EA 7393), 3 rue Fernand Hainaut, 93407 Saint-Ouen, France

1 Introduction

This article deals with the design of large engineering structures made of ductile metals regarding accidental events, e.g. ships collision, bird strike/ingestion in aviation or automotive crashworthiness, which may potentially lead to failure. A *local* defect can have catastrophic consequences on the *global* scale of the structure. Predicting the current residual strength of the overloaded structure is of major interest for preserving the main functions and the integrity of the sensitive areas. Realizing large-scale experiments is associated with unacceptable costs. Instead, it is more favorable to analyze *small-scale* specimens (coupons) extracted from the *large-scale* structure which are exposed to similar conditions and to identify the underlying mechanisms which lead to the propagation of a crack. This work is concerned with the development of a unified physics-motivated numerical model

allowing for virtual failure analysis using the Finite Element Method (FEM).

Describing the overall process of deformation until fracture in ductile materials implies accounting for several interacting mechanisms whose comprehension remains—to this very day—imperfect. One can typically distinguish the following successive steps (often dealt with independently): plastic deformation, diffuse damage, damage concentration (void coalescence) and strain localization, and finally crack formation and propagation.

As a result of void growth induced (diffuse) damage, the material properties are subjected to a progressive degradation. In order to reproduce these effects of ductile damage, several constitutive models have been proposed, e.g. by Gurson (1977), Lemaitre (1985), Rousselier (1987) and also Longère et al. (2012). At an advanced stage of damage evolution, the global structural response migrates to a softening regime (in lieu of the preceding hardening regime). This softening behavior goes along with the concentration of plastic deformation and damage within a narrow band. When using the standard FEM, strain localization manifests itself in a spurious mesh dependence of the structural response. Due to this pathologic behavior, a reliable prediction of the residual strength of the structure after failure can not be provided. Aiming at an estimation which is less conservative and mesh-dependent, the complementary modeling of the post-localization phase is inevitable.

A corrective approach consists in controlling the numerical strain localization in the FE mesh in order to allow for capturing the genuine physical strain localization. The mesh dependence resulting from strain localization can be coped with by introducing a characteristic length into the formulation which serves as localization limiter. Non-local techniques, see e.g. Bažant et al. (1984) and Pijaudier-Cabot and Bažant (1987), can be applied to attenuate the pathology, but accurate results require a very fine mesh and thus a big computational effort for large structures. Moreover, the physical strain localization itself as possible precursor of crack formation can not be properly represented. A promising approach consists in using comparably large FEs and embedding the thin band of highly localized strain into the FE, e.g. by enriching the kinematic FE formulation (Ortiz et al 1987; Belytschko et al 1988) or by enriching the material model (Longère et al 2003). The development of an appropriate (embedded-band) method capable of reproducing the physical localization band is discussed in this paper.

An efficient method to model the void coalescence-induced damage accumulation band in front of the crack tip, which is also referred to as meso-crack, is the cohesive zone model. Cohesive zone models were originally proposed by Barenblatt (1959) and Dugdale (1960) and further extended by Hillerborg et al. (1976). Applications to ductile materials which fail from void nucleation, growth and coalescence were proposed e.g. by Needleman (1987) and Siegmund and Brocks (2000). However, instead of describing the damage mechanisms during strain localization from a microscopic point of view, the (macroscopic) static consequences of strain softening are rather described in a phenomenological way. The degradation process during strain localization is assumed to be lumped into a sufficiently thin cohesive band. Indeed, the cohesive zone allows for a gradual transition between the onset of localization and the formation of a macro-crack. The increasing effect of void coalescence, i.e. the internal necking of the inter-voids bulk material, leads to a decreasing resistance of the material, see Fig. 1. Finally, the stress carrying capacity of the material is completely lost locally and a crack can form.

The X-FEM is considered here as a suitable method to model the cohesive band in the FE mesh. In contrast

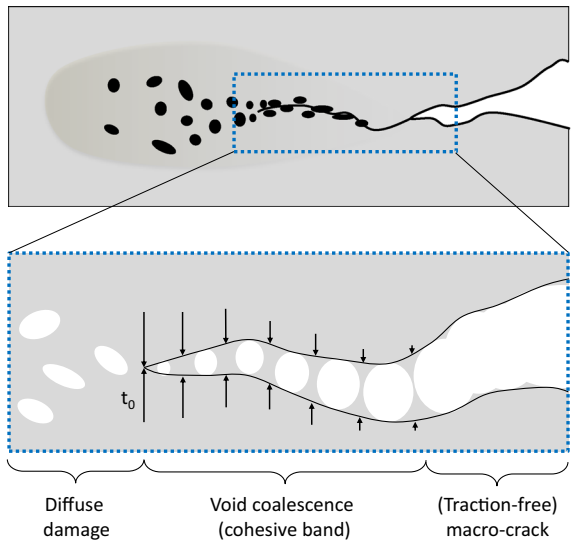

Fig. 1 Visualization of the cohesive zone concept: (*top*) Ductile fracture model, (*bottom*) Introduction of cohesive tractions corresponding to the void coalescence-induced strain localization

to other approaches, as e.g. the commonly used inter-element methods applied in the context of the delamination of composite materials, see e.g. Camanho and Dávila (2002) and Turon et al. (2007), and in the context of ductile materials, see e.g. Xu and Needleman (1994) and Camacho and Ortiz (1996), the X-FEM does not require the a priori knowledge of the crack path on the one hand and extra cohesive elements along this crack path on the other hand. In another context, it does not need expensive remeshing. Indeed, the X-FEM, by enriching the finite element formulation, allows for incorporating the cohesive crack into the mesh independently of the mesh topology. The cohesive band is inserted right at the onset of decohesion so that the problem of assigning a large stiffness to the cohesive zone from the very beginning of the simulation is avoided.

The subject of this article consists in modeling a strain localization induced cohesive band within a unified ductile failure model using the X-FEM implemented into the engineering FE computation code Abaqus.

General considerations necessary for subsequent developments are outlined in Sect. 2. The numerical methodology combining the cohesive band model and the X-FEM to represent the strain localization within the finite element is explained in Sect. 3. A propagation algorithm is developed and two applications considering tensile tests with a single finite element and then a 2D plate are finally discussed in Sect. 4.

2 General considerations and basic concepts

In this section the material constitutive model, the cohesive zone model, the applied enrichment method and the criterion for the onset of strain localization are introduced.

2.1 Material constitutive model

In this work, materials as metals and alloys are considered whose failure results from micro-void growth induced damage, see e.g. Longère et al. (2012). The presented constitutive model accounts for the effects of strain hardening and void growth induced damage.

In order to couple the mechanisms of damage and plasticity, the micromechanics-based Gurson model, see Gurson (1977), later extended by Tvergaard (1981) (also referred to as GTN model) has been retained here. The damage-plastic potential of the GTN model reads

$$\Phi_G = \left(\frac{\sigma_{eq}}{\sigma_y}\right)^2 + 2q_1 f \cosh\left(-\frac{3}{2}q_2\frac{p_m}{\sigma_y}\right) - 1 - (q_1 f)^2 = 0 \tag{1}$$

where q_1 and q_2 are material constants, f is the porosity and σ_{eq} denotes the equivalent stress

$$\sigma_{eq} = \sqrt{\frac{3}{2}\mathbf{s} : \mathbf{s}}. \tag{2}$$

Therein, $\mathbf{s}$ is the deviatoric part of the Cauchy stress tensor $\boldsymbol{\sigma} = \mathbf{s} - p_m\boldsymbol{\delta}$ with the mean pressure p_m and the identity tensor $\boldsymbol{\delta}$. The yield stress σ_y in Eq. (1) is computed from the assumption that only a quasi-static loading is considered so that the effects of viscoplasticity and thermal softening are neglected in this study. A Voce-type strain hardening law is used, as proposed by Longère et al. (2012)

$$\sigma_y = r_0 + \underbrace{r_{\inf}[1 - \exp(-k\kappa)]^{\beta}}_{r(\kappa)}, \tag{3}$$

where $(r_0, r_{\inf}, k, \beta)$ are material constants related to the hardening behavior, κ is the accumulated plastic deformation and $r(\kappa)$ is the exponential hardening function. The evolution of the accumulated plastic deformation is determined from the equality of the macroscopic plastic power with the microscopic one (Gurson 1977) as follows

$$\dot{\kappa} = \frac{\boldsymbol{\sigma} : \dot{\boldsymbol{\varepsilon}}^p}{(1-f)\sigma_y}, \tag{4}$$

where the plastic strain rate is computed from the normality rule

$$\dot{\boldsymbol{\varepsilon}}^p = \dot{\lambda}\frac{\partial\Phi}{\partial\boldsymbol{\sigma}} = \dot{\varepsilon}^{pD}\mathbf{P} + \frac{1}{3}\dot{\varepsilon}^{pM}\boldsymbol{\delta}, \tag{5}$$

where $\dot{\varepsilon}^{pD} = \dot{\lambda}\frac{\partial\Phi}{\partial\sigma_{eq}}$ and $\dot{\varepsilon}^{pM} = -\dot{\lambda}\frac{\partial\Phi}{\partial p_m}$ represent, respectively, the distortional and dilatational parts of the plastic strain rate $\dot{\boldsymbol{\varepsilon}}^p$, $\mathbf{P} = \frac{3}{2}\frac{\mathbf{s}}{\sigma_{eq}}$ is the direction of isochoric plastic flow and $\dot{\lambda}$ is the plastic multiplier. The porosity is assumed to evolve from the superposed effects of the growth of existing voids ($\dot{f}_g$) and the nucleation of new voids ($\dot{f}_n$): $\dot{f} = \dot{f}_g + \dot{f}_n$. The growth of voids can be computed from the hydrostatic plastic deformation

$$\dot{f}_g = (1-f)\dot{\varepsilon}^{pM} \tag{6a}$$

$$f_g(0) = f_0 \tag{6b}$$

The nucleation of new voids is described by a probabilistic function using the Gaussian-type distribution of Chu and Needleman (1980)

$$\dot{f}_n = A_n\dot{\kappa}; \quad \mathrm{A_n} = \frac{\mathrm{f_N}}{\mathrm{s_N}\sqrt{2\pi}}\exp\left[-\frac{1}{2}\left(\frac{\kappa-\kappa_\mathrm{N}}{\mathrm{s_N}}\right)^2\right] \tag{7a}$$

$$f_n(0) = 0 \tag{7b}$$

with $\{f_N, s_N, \kappa_N\}$ being material parameters. In order to take into account the experimentally observed void growth under pure shear loading, an advanced formulation of the plastic potential proposed by Longère et al. (2012) has been chosen. Therein, a variable equivalent to a kinematic pressure p_r is introduced into the GTN potential. Instead of using a logarithmic function, here a linear function is proposed in order to improve the numerical stability

$$p_r = b(q_1 f - 1), \tag{8}$$

with b being a positive material constant. This variable provokes a shift of the yield surface towards positive pressures so that the modified potential takes the form

$$\Phi_G^{mod} = \left(\frac{\sigma_{eq}}{\sigma_y}\right)^2 + 2q_1 f\cosh\left(-\frac{3}{2}q_2\frac{p_m+p_r}{\sigma_y}\right) - 1 - (q_1 f)^2 = 0 \tag{9}$$

The GTN model involving isotropic strain hardening is numerically integrated using the radial return algorithm, see Aravas (1987). The integration is based on a separate consideration of the deviatoric and the hydrostatic part.

2.2 Cohesive zone model

Cohesive models are characterized by two constitutive relations: the classical stress-strain-relation (volumetric) describing the bulk material that remains continuous and an additional cohesive law which relates the traction force t to the displacement jump $[[u]]$ between the cohesive band faces, see Fig. 2 (explained in detail below). The cohesive law is defined by the cohesive strength t_0, the decohesion energy per unit area W_c and its shape.

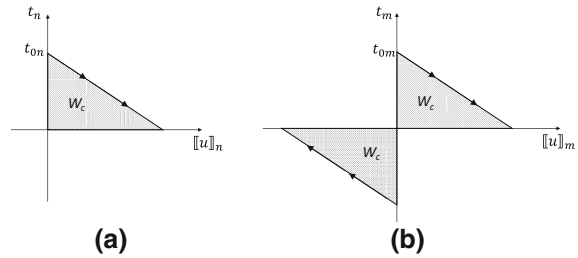

Fig. 2 Applied linear softening cohesive laws in the **a** normal and **b** tangential direction

The initiation of the progressive material separation (within the X-FEM) is usually triggered when the maximum tensile stress attains the maximum cohesive traction t_0. In this work, however, decohesion is assumed to initiate when a stability criterion deduced from bifurcation analysis is satisfied. In such a case, the initial cohesive strength is no longer a material parameter but rather results from the current stress state at the onset of localization so as to provide a smooth transition. Thus the activation of the cohesive band is naturally provided by the material model and accounts for the loading path. After the onset of localization, the behavior in the cohesive band is determined from the traction-separation law. A linear softening law is adopted here due to its simplicity and its frequent use in the context of ductile materials, see e.g. Tvergaard and Hutchinson (1992), Li and Chandra (2003) and Gullerud et al. (2000).

It is well known that ductile damage is driven by void growth (favored by hydrostatic tension) and the ultimate stage of damage occurs in the form of void coalescence (favored by both hydrostatic tension and deviator). Therefore the propagation of the process of localization involves a cohesive law which accounts for a normal and also a (in-plane) shear component, i.e.

$$t = t_n\mathbf{n} + t_m\mathbf{m}, \tag{10}$$

where $\mathbf{n}$ and $\mathbf{m}$ denote, respectively, the normal and tangential vector of the cohesive band.

Figure 3 shows a post-mortem tension specimen made of ductile material. It can be seen that the opening Mode I is predominant in the specimen width whereas the shearing Mode II is predominant in the thickness. While numerically simulating such a tension test assuming 2D conditions for e.g. assessing the performance of a new development (of a constitutive model, of a numerical methodology, etc.), plane stress

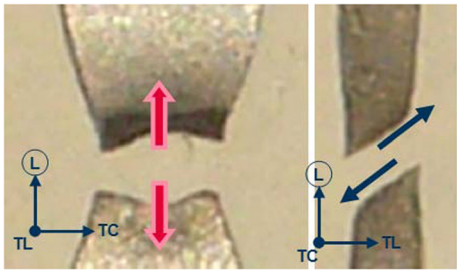

Fig. 3 Rupture of a ductile plate during a uni-axial tensile test: (*left*) rupture in the predominant opening mode in the plate width and (*right*) rupture in the predominant shear mode in the plate thickness

hypothesis (small thickness, as for the left picture of Fig. 3) is expected to activate Mode I crack propagation, and plane strain hypothesis (large thickness, as for the right picture of Fig. 3) is expected to activate Mode II crack propagation.

Under the 2D-plane strain condition assumed in the present work (thick plate, corresponding to the right picture of Fig. 3), the cohesive band is supposed to cross the plate entirely in its thickness (i.e. the width of the tension specimen in Fig. 3). In order to be able to describe both effects of hydrostatic tension and shear on void coalescence (in the form of void impingement and localized shearing), the cohesive law has to take into account tension and shear components, see Fig. 2. The cohesive law considered here is expressed as

$$t_m = t_{0m} - \mathrm{sign}(t_{0m})\frac{t_{0m}^2}{2W_c}\left|[[u]]_m\right| \tag{11}$$

$$t_n = t_{0n} - \frac{t_{0n}^2}{2W_c}[[u]]_n, \tag{12}$$

where it is tentatively assumed that the work of separation per unit area W_c is the same in tension and shear. The maximum tractions t_{0n} and t_{0m} are evaluated at the onset of localization from the current stress state. The unloading behavior is not particularly treated here as the applications considered in this work refer mostly to monotonically increasing loading path.

2.3 Enrichment method

The principles of the classical X-FEM reproducing a stress-free crack and the adopted approach in the present work are presented in the following section.

2.3.1 *Principle of the X-FEM*

Instead of refining the mesh around the crack lips and tip to resolve the singular stress field, the displacement field is enriched by a priori defined functions which represent the crack discontinuity and singular stress field. Thus, the crack is expected to propagate independently of the mesh.

The X-FEM is used to embed a discontinuity function into the element formulation by adding to the regular displacement field $u_{reg}(x)$ enrichment functions which represent the kinematical consequences of the entity at the origin of the discontinuity

$$u(x) = u_{reg}(x) + u_{dis}(x) + u_{sing}(x), \tag{13}$$

where u_{reg} represents the regular (standard) finite element displacement, u_{dis} the discontinuous displacement field across the discontinuity and u_{sing} the crack tip displacement field resulting from a singular stress. These three terms can be interpolated as follows

$$u_{reg}(x) = \sum_{i\in I} N_i(x)a_i \tag{14}$$

$$u_{dis}(x) = \sum_{j\in J} N_j(x)H(x)b_j \tag{15}$$

$$u_{sing}(x) = \sum_{k\in K} N_k(x)\left(\sum_{l=1}^{4} c_k^l F_l(r,\theta)\right) \tag{16}$$

where I, J, K represent the set of all nodes belonging to, respectively, the structure mesh/ the cut elements/ the elements containing the crack tip. The degrees of freedom a_i, b_j and c_k correspond to the regular, discontinuous and singular displacement field and generally are the unknowns of the FE analysis. $H(x)$ is the Heaviside function, which is determined from the signed distance function from the crack $d(x)$ such that $H(x) = \mathrm{sign}(\mathrm{d}(\mathrm{x}))$. The Heaviside function takes the value $+1$ for a point which is located above the crack and -1 for a point which is located below the crack. F_l are the asymptotic crack tip functions, formulated using the polar coordinates r (distance from crack tip) and θ (polar angle), see Fig. 4. Under the hypothesis of an elastic or quasi-brittle material behavior, these enrichment functions can be derived analytically from the Westergaard solutions, see Westergaard (1939) and Belytschko and Black (1999),

$$F_l(r,\theta) = \left[\sqrt{r}\sin\frac{\theta}{2}, \sqrt{r}\cos\frac{\theta}{2}, \sqrt{r}\sin\theta\sin\frac{\theta}{2}, \sqrt{r}\sin\theta\cos\frac{\theta}{2}\right] \tag{17}$$

where the term $\sqrt{r}$ leads by differentiation to a singular strain and stress field involving the term $\frac{1}{\sqrt{r}}$, which converges to infinity when approaching the crack tip $r \to 0$. It should be noted that only the nodes belonging to the elements which are fully cut (enrichment with Heaviside function) or contain the crack tip (enrichment with singular functions) are enriched.

2.3.2 Adopted approach

In the case of a strongly non-linear elasto-plastic ductile material, as it is the case in this work, the singular terms in the enhanced displacement formulation can be neglected, see Crété et al. (2014). Therefore the number of degrees of freedom can be drastically reduced without losing accuracy. Then the enriched displacement field can be rewritten as follows

$$u(x) = \sum_{i\in I} N_i(x)a_i + \sum_{j\in J} H(x)N_j(x)b_j. \tag{18}$$

The shifted basis formulation is applied here, originally proposed by Zi and Belytschko (2003). By using the shifted basis formulation, the enrichment term vanishes at the nodes and thus avoids the cumbersome use of blending elements (transition elements between the enriched elements and the standard finite elements) leading to an optimal convergence rate. In the shifted basis approach, the Heaviside function at the nodes H_j is taken into account and thus only the cut elements are enriched

$$u(x) = \sum_{i\in I} N_i(x)a_i + \sum_{j\in J} \big(H(x) - H_j\big)N_j(x)b_j. \tag{19}$$

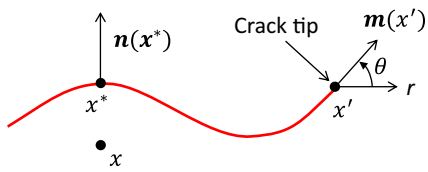

Fig. 4 Crack surface characterized by the normal vector **n** at point x^* on the crack and the crack tip at point x' using a polar coordinate system

The enrichment function H is calculated from the level set function ϕ which captures the crack trajectory and needs to be updated when the crack propagates.

2.4 Onset and direction of the strain localization band

It is assumed here that strain localization is induced by void coalescence and that its initiation can be determined from bifurcation analysis which is adapted for rate-independent materials considered in this work. Thus the transition from diffuse damage to the formation of a localization band relies on finding a condition for the spontaneous occurrence of an inhomogeneous strain mode within a homogeneous material. The elaboration of such a condition is the fruit of the early works of Hadamard (1902), Thomas (1957), Hill (1958) and Mandel (1966). The bifurcation analysis consists in evaluating the orientation of the localization band **n** for which the determinant of the acoustic tensor **Q** becomes zero (or numerically negative) for the first time, i.e.

$$\det \mathbf{Q}(\mathbf{n}) = \det(\mathbf{n}\cdot\mathbf{D}^{\mathbf{t}}\cdot\mathbf{n}) = 0, \tag{20}$$

Normally, two solutions for **n** are found.

3 Combining cohesive models and X-FEM

The principle of combining a strong discontinuity cohesive model within the X-FEM framework is discussed in this section.

The developed set of discrete linearized equations of the X-FEM including a cohesive band, see e.g. Wells and Sluys (2001), is given in the following incremental form

$$\mathbf{K}\begin{Bmatrix} \mathrm{d}a \\ \mathrm{d}b \end{Bmatrix} = \begin{Bmatrix} \mathbf{f}_a^{ext} \\ \mathbf{f}_b^{ext} \end{Bmatrix} - \begin{Bmatrix} \mathbf{f}_a^{int} \\ \mathbf{f}_b^{int} \end{Bmatrix}, \tag{21}$$

where the tangent stiffness matrix **K** is computed as follows

$$\mathbf{K} = \begin{bmatrix} \int_\Omega \mathbf{B}^T\mathbf{D}^{\mathbf{t}}\mathbf{B}\,\mathrm{d}\Omega & \int_\Omega \mathbf{B}^T\mathbf{D}^{\mathbf{t}}\mathbf{B}^*\,\mathrm{d}\Omega \\ \int_\Omega \mathbf{B}^{*T}\mathbf{D}^{\mathbf{t}}\mathbf{B}\,\mathrm{d}\Omega & \int_\Omega \mathbf{B}^{*T}\mathbf{D}^{\mathbf{t}}\mathbf{B}^*\,\mathrm{d}\Omega + 4\int_{\Gamma_D}\mathbf{N}^T\mathbf{T}\mathbf{N}\,\mathrm{d}\Gamma \end{bmatrix}, \tag{22}$$

Therein, the **B**-matrix contains the spatial derivatives of the shape functions **N**, i.e. $\mathbf{B} = \mathbf{L}\mathbf{N}$ with **L** being the matrix differential operator

$$\mathbf{L} = \begin{bmatrix} \partial/\partial x & 0 \\ 0 & \partial/\partial y \\ \partial/\partial y & \partial/\partial x \end{bmatrix} \tag{23}$$

and $\mathbf{B}^* = \mathbf{L}\mathbf{N}^*$ with $\mathbf{N}^*$ containing the entries $N_j^* = (H(x) - H_j)N_j$ for each node j of the enriched element. Furthermore, $\mathbf{D}^{\mathbf{t}}$ denotes the elastic-plastic tangent operator of the microporous plasticity GTN model, see e.g. Huespe et al. (2009), and Γ_D represents the cohesive band discontinuity. The elastic-plastic tangent operator can be deduced from the rate form of the stress-strain relation

$$\dot{\boldsymbol{\sigma}} = \mathbf{D}^{\mathbf{t}} : \dot{\boldsymbol{\varepsilon}}. \tag{24}$$

The components of the internal and external force vectors $\mathbf{f}^{ext}$ and $\mathbf{f}^{int}$ are calculated from

$$\mathbf{f}_a^{ext} = \int_{\Gamma_t} \mathbf{N}^T \mathbf{t}^* \, \mathrm{d}\Gamma \tag{25a}$$

$$\mathbf{f}_b^{ext} = \int_{\Gamma_t} \mathbf{N}^{*T} \mathbf{t}^* \, \mathrm{d}\Gamma \tag{25b}$$

$$\mathbf{f}_a^{int} = \int_{\Omega} \mathbf{B}^T \boldsymbol{\sigma} \, \mathrm{d}\Omega \tag{25c}$$

$$\mathbf{f}_b^{int} = \int_{\Omega} \mathbf{B}^{*T} \boldsymbol{\sigma} \, \mathrm{d}\Omega + 2 \int_{\Gamma_D} \mathbf{N}^T \mathbf{t} \, \mathrm{d}\Gamma, \tag{25d}$$

where the volume forces have been neglected. Therein, $\mathbf{t}^*$ are external traction forces applied at the boundary Γ_t and $\mathbf{t}$ is the traction vector determined from the enriching degrees of freedom

$$\dot{\mathbf{t}} = \mathbf{T}[[\dot{\mathbf{u}}]] = 2\mathbf{T}\mathbf{N}\dot{\mathbf{b}}, \tag{26}$$

where $\mathbf{T}$ is the cohesive tangent modulus as detailed in Eq. (28) below.

It should be noted that the cohesive tangent modulus $\mathbf{T}$ as well as the tractions $\mathbf{t}$ are defined in the local coordinate system of the oriented cohesive band. Therefore it is necessary to perform a transformation from the local to the global system. This is done by taking into account the rotation matrix $\mathbf{R}$ such that

$$\mathbf{t}^g = \mathbf{R}^T \mathbf{t}^l \text{ and } \mathbf{T}^g = \mathbf{R}^T \mathbf{T}^l \mathbf{R} \text{ ; with}$$
$$\mathbf{R} = \begin{bmatrix} \cos\theta & \sin\theta \\ -\sin\theta & \cos\theta \end{bmatrix}, \tag{27}$$

where g denotes the global, l the local coordinate system and θ is the angle according to Fig. 5.

Using the linear softening traction-separation law from Sect. 2.2 yields the following (local) cohesive tangent modulus

$$\mathbf{T}^{\mathbf{l}} = \frac{\partial \mathbf{t}^l}{\partial [[u]]^l} = \begin{bmatrix} \dfrac{\partial \mathbf{t}_m^l}{\partial [[u]]_m^l} & \dfrac{\partial \mathbf{t}_m^l}{\partial [[u]]_n^l} \\ \dfrac{\partial \mathbf{t}_n^l}{\partial [[u]]_m^l} & \dfrac{\partial \mathbf{t}_n^l}{\partial [[u]]_n^l} \end{bmatrix} = \begin{bmatrix} T_m^l & 0 \\ 0 & T_n^l \end{bmatrix}, \tag{28}$$

where the normal and tangential traction components are assumed to be uncoupled from each other. That means that a separation in normal direction does not have an influence on the tangential direction.

The contribution of the continuum domain to the equilibrium equations of an element which is crossed by the localization band is tentatively integrated by subdividing the element into 16 rectangles which are themselves integrated by a standard 4-point Gauss rule. This 64-fixed points scheme, see also Elguedj et al. (2006), Crété et al. (2014) and Fig. 6, is especially adapted to strongly non-linear ductile materials so as to avoid the cumbersome and numerically error-prone projection of loading- and history-dependent internal variables inherent to the classical subtriangulation methods, see e.g. Moës et al. (1999). This method will be used tentatively. Later on, a different method is considered which is particularly efficient when further dealing with large engineering structures.

The integration of the contributions of the cohesive band to the equilibrium equations, i.e. the terms involving a line integral over Γ_D, is effectuated by a standard 2-point Gauss rule, see Fig. 6. Two integration points are necessary, because the displacement jump along the cohesive band is described by a linear interpolation function provided by the X-FEM. As

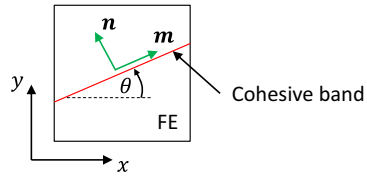

Fig. 5 Global and local coordinate systems of the cohesive band within the FE

opposed to that, the E-FEM (elemental enrichment FEM), see e.g. Oliver (1996), Huespe et al. (2009), requires only one integration point as the enriching degree of freedom is constant over the enhanced element.

In order to update the cohesive tractions at the two Gauss points, the radial return method can be applied in the same way as in the context of plasticity, see e.g. Belytschko et al. (2003) and Simo and Hughes (2006). The normal cohesive tractions are computed according to Algorithm 1.

Algorithm 1 Radial return method to update the (local) normal tractions from pseudo-time step k to $k+1$

1: $[\![u]\!]_n^{k+1} = \mathbf{n} \cdot [\![u]\!]^{k+1} = \mathbf{n} \sum_{i=1}^{4} N_i(\xi,\eta) b_i^{k+1}$
2: **if** $[\![u]\!]_n^{k+1} > 0$ **then** ▷ Contact condition
3: $t_y^{k+1} = t_{0n} + T_n [\![u]\!]_n^{k+1}$ ▷ Current cohesive traction
4: $t_n^{trial} = t_n^k + T_n([\![u]\!]_n^{k+1} - [\![u]\!]_n^k)$ ▷ Prediction step
5: $f^{k+1} = t_n^{trial} - t_y^{k+1}$ ▷ Trial cohesion function
6: **if** $f^{k+1} \geq 0$ **then**
7: $t_n^{k+1} = t_y^{k+1}$ ▷ Correction step
8: **return** t_n^{k+1}, $[\![u]\!]_n^{k+1}$

In case of contact, i.e. $[[u]]_n^{k+1} \leq 0$, the cohesive band is inactive and the material behavior is computed using the equations of motion (Belytschko et al 2003). The tangential tractions are calculated in the same way (index n replaced by m), however the contact condition is not necessary as the shearing can take place in the positive and negative direction. The effect of friction during contact and gliding motion is tentatively neglected.

4 Application

The previous parts have introduced the methodology of coupling a cohesive band method within the X-FEM allowing for dealing with the progressive transition phase of strain localization. The difficulty of applying the method to non-linear ductile materials was carved out and appropriate numerical tools were proposed. The objective of this section is to apply the elaborated combination of cohesive band model and X-FEM to two test cases in order to assess its performance with regard to numerical simulations.

In the following, two different 2D models are studied. The first one is a simple test case using one single FE which serves as means to better understand

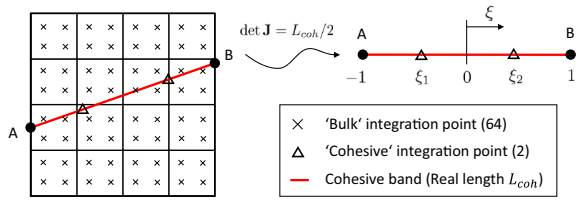

Fig. 6 Tentative integration scheme for a 2D quadrilateral element crossed by a cohesive band: (*left*) FE with 64 fixed Gauss points for the bulk part and 2 Gauss point for the cohesive part, (*right*) Transformed cohesive line element in the natural (local) coordinate ξ

the methodology and analyze potential occurring numerical issues. The second test case concerns a parametric study of a plate which is loaded in tension. An advanced method for the propagation of the cohesive band and crack is proposed and implemented as user element (UEL) in the commercial FE computation software Abaqus (implicit integration scheme). The 2D models are implemented assuming plane strain conditions. The small strain hypothesis is assumed here. The quasi-static loading is applied by displacement control. The modified GTN model detailed in Sect. 2.1 is used. The parameters of the material model are given in the Tables 1 and 2. Therein E denotes the Young's modulus and ν the Poisson's ratio characterizing the elastic material behavior.

4.1 Tensile test using a single 2D FE

Consider the single 2D FE in Fig. 7. Prior to localization, the stress and deformation are uniformly distributed over the element. The onset of localization is detected by using bifurcation analysis evaluated at the Gauss points. If the bifurcation criterion (20) is satisfied, a cohesive band is embedded into the element and assumed to pass through the element center.

The internal forces at the onset of localization read

$$\mathbf{f}_b^{int,0} = \underbrace{\int_\Omega \mathbf{B}^{*T} \boldsymbol{\sigma} \, \mathrm{d}\Omega}_{\mathbf{f}_b^{xfem,0}} + 2 \underbrace{\int_{\Gamma_D} \mathbf{N}^T \mathbf{t}^g \, \mathrm{d}\Gamma}_{\mathbf{f}_b^{coh,0}} . \tag{29}$$

In order to ensure a smooth transition at the onset of localization, $\mathbf{f}_b^{int,0}$ is enforced to be zero, so that follows: $\mathbf{f}_b^{coh,0} = -\mathbf{f}_b^{xfem,0}$. This implies that the initial tractions are not calculated directly, but rather the

internal cohesive force which compensates the internal force of the bulk associated to the enriching degrees of freedom in order to entirely cancel out the liberty provided by the X-FEM. In order to provide such a condition, the cohesive law has to be shifted to negative tractions, so that the initial cohesive traction vanishes, i.e. $t_0 = 0$. Finally, the internal force of the cohesive band reads

$$\mathbf{f}_b^{coh} = -\mathbf{f}_b^{xfem,0} + \Delta\mathbf{f}_b^{coh} \; ; \text{with } \Delta\mathbf{f}_{\mathrm{b}}^{\mathrm{coh}} = 2\int_{\Gamma_{\mathrm{D}}} \mathbf{N}^{\mathrm{T}}\mathbf{t}^{\mathrm{g}}\,\mathrm{d}\Gamma \tag{30}$$

4.2 Tensile test of a 2D plate

In this section a 2D plate specimen is considered which is subjected to a quasi-static tension loading. The objective of this test case is to propose and test an algorithm for cohesive band propagation and crack formation.

4.2.1 Problem statement

Consider the plane specimen in Fig. 8 which is fixed at the bottom and loaded in tension at the top (in red). The imposed displacement is increased quasi-statically up to a value U_{max}. The thickness of the plate is 1 mm. The plate is free of pre-cracks so that a strategy will be proposed which identifies the position of the first nucleation of the localization band. Plane strain conditions are assumed here. The illustrations of the results are restricted to the area of interest (see the dashed box in Fig. 8) where the propagation of the cohesive band takes place.

Ten different simulations are conducted, see Table 3. In the table short cuts are assigned to the simulations (first column) serving as references for later discussion. In order to analyze the sensitivity to the mesh size, two different element sizes are used: about 0.5 mm element size for the coarse mesh and 0.25 mm for the fine mesh. Furthermore, the cohesive tangent moduli $T_m^l = T_n^l$ in Eq. (28) are varying. And

Table 1 Parameters related to the elastic and strain hardening laws

E	v	r_0	r_{inf}	k	β
200 GPa	0.33	300 MPa	350 MPa	4.4	0.5

Table 2 Parameters related to the microporous plasticity GTN model

q_1	q_2	f_0	f_N	s_N	κ_N	b
1	1	10^{-3}	0.04	0.05	0.3	100 MPa

then, in the next section, a new propagation method combined with a 4-point Gauss rule is presented, so that simulations with 64 and also 4 GP are employed and compared. Furthermore, two simulations are employed with the GTN model without discontinuity. Finally, two simulations are conducted—one with a fine mesh and one with a coarse mesh—using the X-FEM only, i.e. without a cohesive zone model (CZM).

4.2.2 Description of the propagation algorithm

The propagation of the cohesive band, then the crack formation, is accomplished by the sequence of the following four steps

1. Onset and direction of propagation of the cohesive band
2. Determination of the propagation length
3. Propagation of the cohesive band
4. Onset of the macro-crack in the cohesive band wake

The methodology is explained below step by step. It is assumed that only one cohesive band can propagate throughout the structure. Branching can occur in

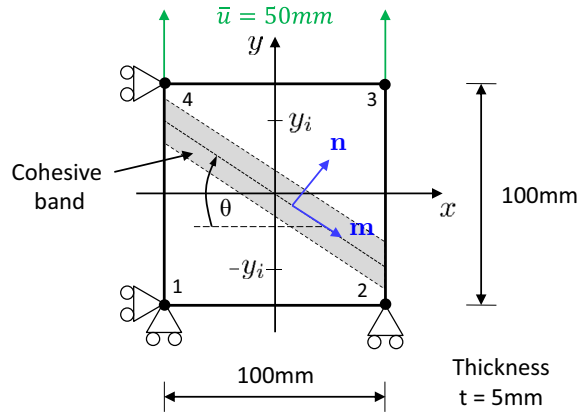

Fig. 7 Tensile loading of a single 2D FE with a slanted cohesive zone inserted at the onset of strain localization

ductile materials, but it is not considered here. A flow chart of the propagation algorithm is given at the end of this section in Fig. 12.

4.2.2.1 Onset and direction of propagation of the cohesive band The bifurcation condition (20) is evaluated locally at an additional Gauss point which is inserted at the element center and does not contribute to the global equation system, i.e. its weight is negligibly small. The space between 1 and 180 degrees is swept by increments of 1 degree. For each orientation the bifurcation criterion is checked. If this criterion is fulfilled, the angle is added to a list. Then, within this list the propagation angle corresponding to the smallest determinant value is chosen. Various criteria are checked to verify if that angle is numerically and physically appropriate (e.g. if the direction would lead to overlapping of the existing band or if a crossed element would be cut twice). If the propagation angle does not fulfill these criteria, the angle with the second smallest determinant value is selected and so on until an appropriate angle is found.

The cohesive band is inserted only once the porosity at the center GP exceeds a critical value. This criterion is necessary to ensure that already some damage has evolved in the element before it is localized and thus prevents from premature artificial localization. Based on purely numerical reasons, its value is set to $f_{ini} = 0.03$ which is found to be a good compromise between numerical and physical aspects. A double criterion has thus to be satisfied for the cohesive band activation:

1. the bifurcation condition is met at the center GP of the element located in front of the current cohesive band
2. the central porosity has reached a critical value at the center GP.

This is a tentative approach as it is well known that a local evaluation of the initiation criterion may lead to pathological mesh dependence, see e.g. Longère et al. (2012). A more appropriate (non-local) methodology for ductile material has been proposed by Crété et al. (2014) and may be implemented in future works.

Due to the fact that the specimen is initially free of defects or cracks, an approach is proposed which allows to find the element where the cohesive band nucleates, see Fig. 9. A loop over all elements identifies all those which fulfill the aforementioned criteria. If several such elements are found (what is normally the case), the cohesive band nucleates in the element with the largest porosity at the center GP.

4.2.2.2 Propagation of the cohesive band When the cohesive band is inserted into the element, the initial cohesive tractions of the cohesive law are not computed from the stress state, but the third approach at the end of Sect. 4.1 is applied to avoid

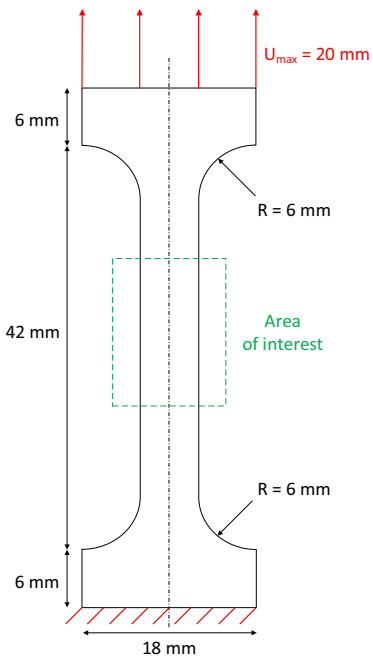

Fig. 8 Model of the plane uncracked specimen subjected to a quasi-static displacement loading U_{max}

Table 3 Configurations of the employed simulations

Short cut	Mesh	No. of GP	T_n^l/T_m^l(N/mm^3)
Sim1	Fine	4	−25.0
Sim2	Fine	4	−12.5
Sim3	Coarse	64	−25.0
Sim4	Coarse	64	−12.5
Sim5	Coarse	4	−25.0
Sim6	Coarse	4	−12.5
Sim7	Fine	4	No discontinuity
Sim8	Coarse	4	No discontinuity
Sim9	Fine	4	X-FEM without CZM
Sim10	Coarse	4	X-FEM without CZM

serious convergence problems. Instead of prescribing the fracture energy, the cohesive moduli are given due to a better numerical performance. The normal and tangential cohesive moduli in Eq. (28) are assumed to be equal, i.e. $T_m^l = T_n^l$.

Several modifications of the constitutive bulk behavior are made in order to better agree with physics and improve numerical performance. First of all, the void growth is enforced to stagnate at the continuum GPs in the elements which are crossed by the cohesive band. This can be justified physically because the cohesive band is assumed to be the narrow zone where all the damage and plasticity processes are henceforth concentrated. It corresponds also to the experimental observations which suggest that around the meso-crack there are only a few small voids, see also Longère et al. (2012). Therefore, the void growth is reduced to the elements in the process zone. This has also an important numerical advantage as it turned out that the simulation suffers from convergence problems if the void growth is not restricted.

4.2.2.3 Determination of the propagation length How far does the localization band propagate during one displacement increment of the monotonic loading? The characteristics of the propagation velocity for fatigue loading are well studied, see e.g. Pugno et al. (2006), Sukumar et al. (2003) and Krupp (2007). However, in the case of a monotonically increasing loading, far less research can be found. For a slow, quasi-static loading[1], experiments with the ductile material DH36 suggest that the meso-crack propagates intermittently by the length of the mesocrack (about $200 - 300\mu m$, see Longère et al. (2012)). Modeling such a propagation length with FEs would require a prohibitively small element size compared to the structure dimensions. Therefore, the length of the intermittently propagation cohesive segment has to be adapted to the FE mesh. The procedure of that so-called exhaustion method is described below. It corresponds to the approach proposed by Crété et al. (2014) in the context of crack propagation.

The cohesive band is propagating element by element and its orientation does not change within an element. The front of the cohesive band is assumed to be located always on an edge. At first, the cohesive band propagates within the element in front of the current cohesive band as soon as it fulfills the propagation criteria. Then, still in the same increment and without recalculating the equilibrium, the band propagates in the next element if the criteria are fulfilled until exhaustion is attained. Due to convergence issues, the equilibrium is not recalculated when a cohesive band propagates through several elements, as it is done e.g. in the approach proposed by Pourmodheji and Mashayekhi (2012).

4.2.2.4 Onset of the macro-crack in the cohesive band wake Instead of waiting until the residual strength of the cohesive band is completely lost, i.e. both the tractions t_m and t_n are zero, the crack is formed already before. This has two reasons. First of all, this corresponds to the assumption that the interrelating bonds of the coalescing voids can only stand a certain critical or rupture traction. Exceeding this traction leads to a sudden rupture of this ligament and so to the formation of new crack surfaces. Secondly, this approach improves the convergence rate. An effective traction in the local coordinate system $t_{eff} = \sqrt{t_m^{l2} + t_n^{l2}}$ is computed and compared to a critical value, here the—up to now—arbitrary value of 100 MPa is chosen.

4.2.2.5 Considerations on the integration scheme Realizing that a relatively fine mesh has to be used to get reliable results, using 64 Gauss points in each FE from the beginning of the simulation (Elguedj et al 2006; Crété et al 2014) tremendously slows down the calculation time, especially with regard to large structures. Also the subsequent numerical tests have revealed that using 64 GP in combination with a very fine mesh may lead to divergence of the solution. Therefore a different strategy is used here which allows reducing the number of GP tremendously and at once maintaining a still acceptable accuracy.

Here it is proposed to use the standard 4-point Gauss rule. In order to guarantee that at least one Gauss point

[1] In the case of a dynamic load case, the propagation length can be e.g. controlled by empirical laws. Kanninen and Popelar (1985) proposed a power law for elastic matrials. This was extended to elasto-plastic materials by Haboussa et al. (2011) and to void-induced ductile fracture by Crété et al. (2014) using the stored plastic energy in front of the meso-crack tip. One difficulty for the treated ductile materials in this work is the lacking amount of experimental data in the case of dynamic loading.

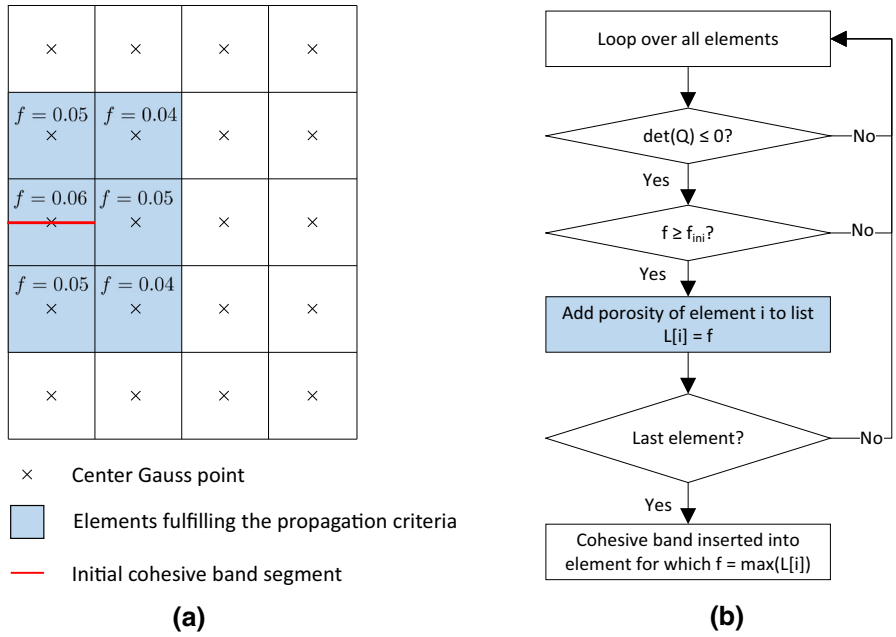

Fig. 9 Strategy to set the initial cohesive band: **a** situation in the FE mesh, **b** algorithm to determine the element containing the initial cohesive band

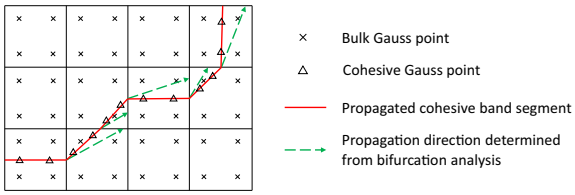

Fig. 10 Modified propagation algorithm using 4 GP in the continuum

is on both sides of the cohesive band, the new cohesive segment is forced to traverse the center of an edge. Depending on the bifurcation angle, the propagation angle can only take three possible values determined by the geometry of the element, see Fig. 10.

The question arises in how far the accuracy of the proposed method is impaired compared to the previously recommended 64-point integration scheme. In the following, the propagation algorithm presented in this chapter is applied to the plate specimen in Fig. 8. In accordance with the objectives of this work, a rather coarse FE mesh is used (element size 0.5 mm). For each method two different values for the cohesive tangent modulus are considered. The results are shown in Fig. 11.

It can be observed that the difference between the global responses of the two approaches is slight and independent of the cohesive law. This startling finding

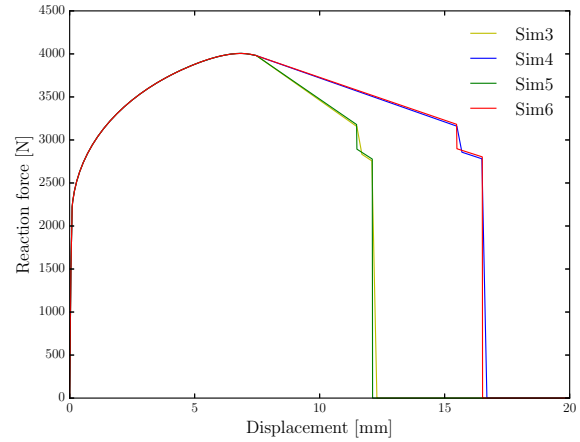

Fig. 11 Evolution of the reaction force with coarse mesh for Sim3, Sim4, Sim5 and Sim6, see Table 3 for the nomenclature

implies that the costly use of the 64-point Gauss rule in each FE from the beginning of the simulation can be replaced by the standard 4-point rule without losing any accuracy. Although the propagation algorithm has to be slightly modified, this seems to be an efficient approach applicable to large engineering structures requiring a coarse mesh. The advantages of using 4 Gauss points instead of 64 Gauss points can be summarized as follows:

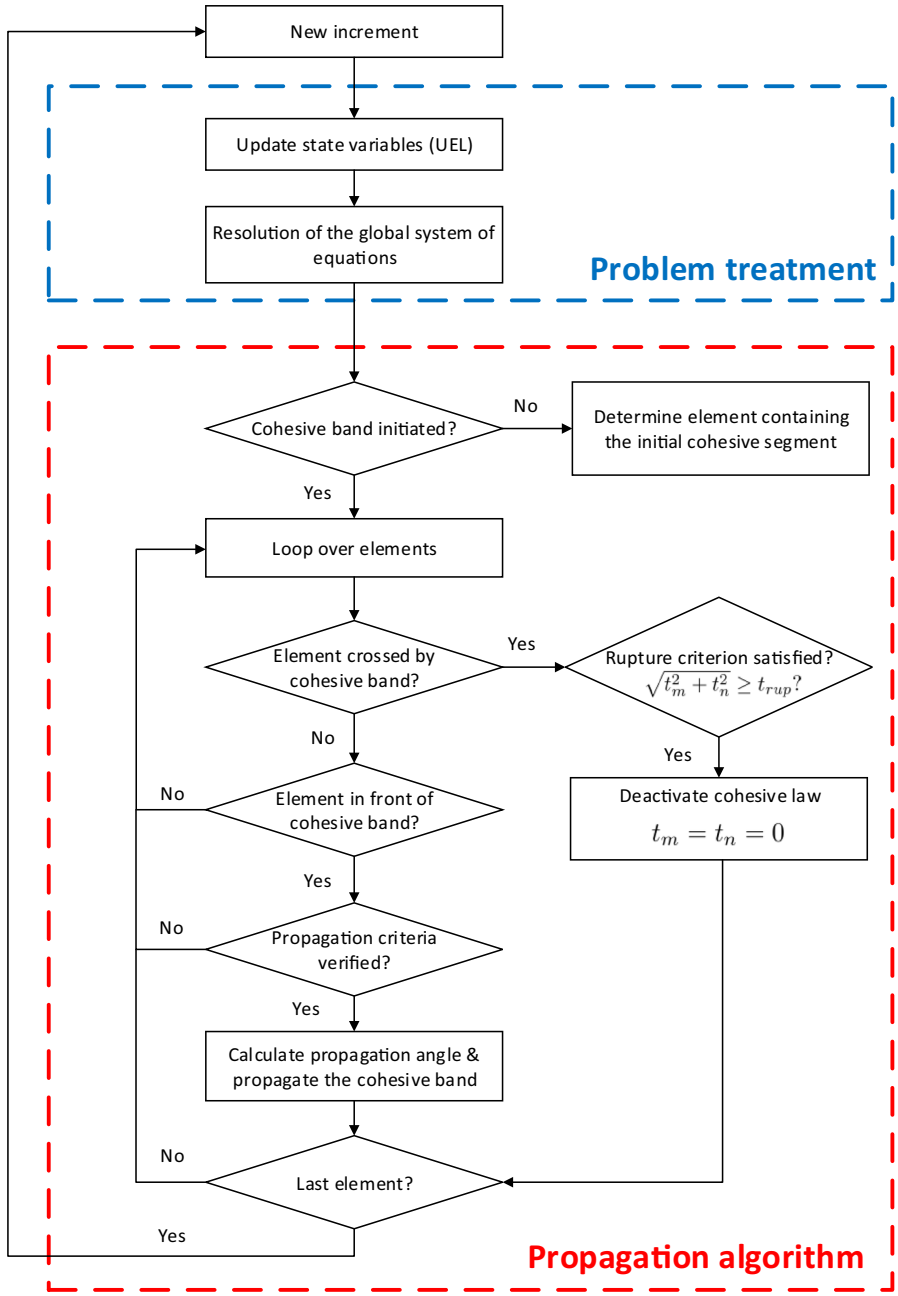

Fig. 12 Flow chart of the propagation algorithm

– It is considerably faster.
– It requires much less storage for the state variables on each Gauss point and thus much less time for post-processing.
– It is numerically more stable, because simulations with the 64-point rule has revealed convergence problems when applied to a very fine mesh.
– It provides still a good prediction of the global response.

The 4-point Gauss integration in combination with the described propagation algorithm is therefore used in the following.

4.2.2.6 Summary of the algorithm The algorithm is summarized as a flow chart in Fig. 12. The propagation of the cohesive band and/or the crack is done at the end of a displacement increment. Therefore the introduction of a discontinuity into the unbalanced

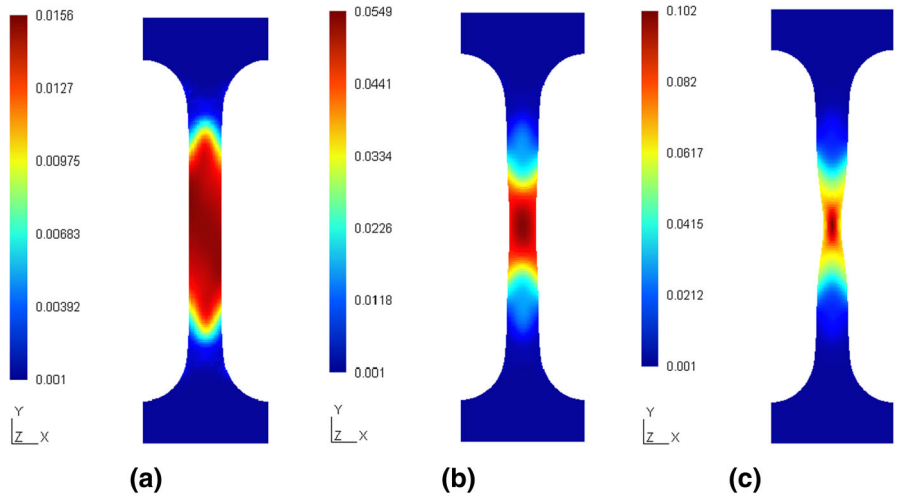

Fig. 13 Localization of damage f with Sim7, see Table 3 for the nomenclature, at different loading states: **a** $U = 7.1\,mm$, **b** $U = 8.2\,mm$, **c** $U = 9.9\,mm$

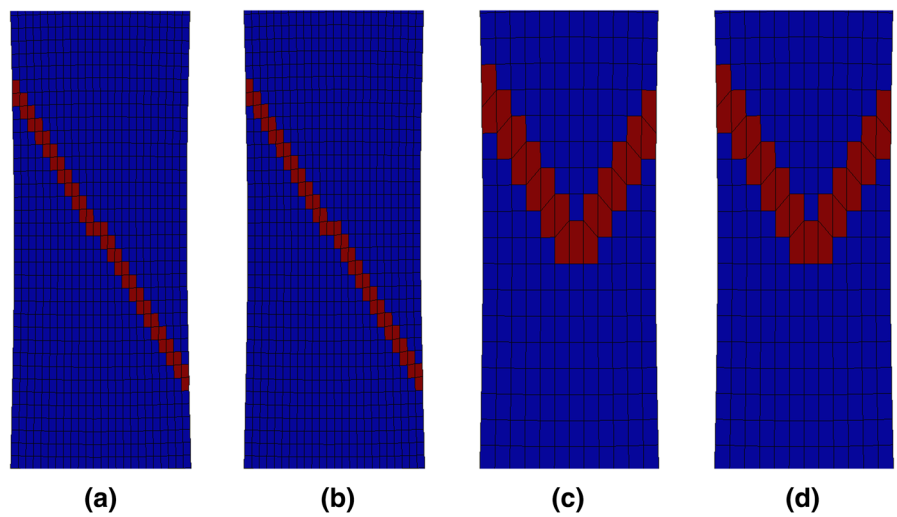

Fig. 14 Propagation angle of the cohesive band at an early stage of localization ($U = 7.8\,mm$): **a** Sim1, **b** Sim2, **c** Sim5, **d** Sim6, see Table 3 for the nomenclature

system during iteration can be avoided and the optimal convergence rate of the Newton-Raphson solution scheme can be maintained.

4.2.3 Results

The results of the simulations in Table 3 are discussed here. The visualization of the simulations is employed with the software Gmsh (Geuzaine and Remacle 2009). According to the 2D-plane strain condition assumed here, the band which will later give birth to the crack is expected to propagate following Mode II, i.e. with an angle of around 45° with respect to the normal of the loading direction, as for the right picture of Fig. 3 (see comments above that figure).

4.2.3.1 Localization of damage and specimen necking using the GTN model If the GTN model is used throughout the entire simulation without numerically treating the phase of strain localization, the damage and plasticity concentrates within a few FEs located in the center of the specimen, see Fig. 13. The latter shows specimen necking and no thin band of heterogeneous deformation, which is clearly in contradiction with the experimental results (see right picture of Fig. 3). As a consequence, the use of only a continuous model throughout the entire failure process

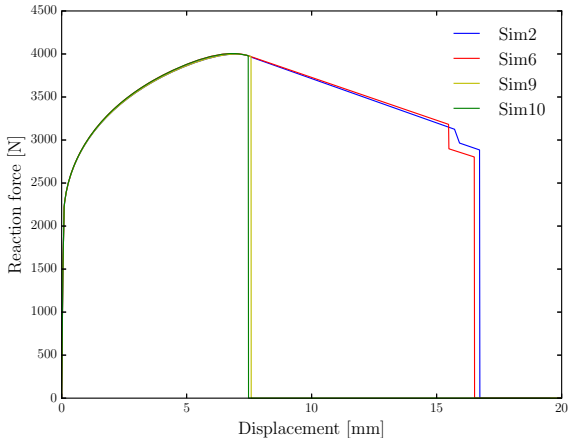

Fig. 15 Evolution of the reaction force for Sim2, Sim6, Sim9 and Sim10, see Table 3 for the nomenclature

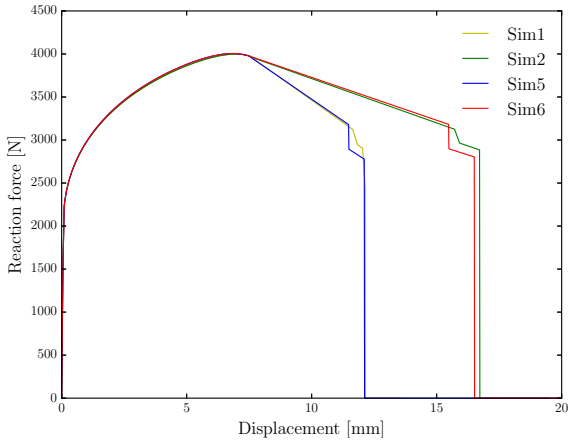

Fig. 17 Evolution of the reaction force for Sim1, Sim2, Sim5 and Sim6, see Table 3 for the nomenclature

does not allow for reproducing the phase of void coalescence-induced localization band and further Mode II-crack propagation in the specimen thickness.

4.2.3.2 Comparison of the propagation angle At the onset of localization, the cohesive band is inserted into the structure. It is observed that in all simulations the cohesive band nucleates in the very center of the structure and then propagates towards both sides, see Fig. 14.

The first two simulations a) and b) show the propagation within a fine mesh but different tangent moduli. The cohesive band propagates as one line through the structure and with an angle of 58° with respect to the horizontal axis as the result of the bifurcation criterion. This numerical value of 58° has to be compared with the experimental value of 45° reported previously (see above and right picture of Fig. 3). This discrepancy may be explained by the hypothesis of 2D-plane strain condition assumed for the numerical simulations while not being satisfied for the real loading case (the width of the tension specimen is not large enough for the plane strain condition to be met). Changing the stiffness of cohesive band does not have an influence on the propagation angle. In contrast to the fine mesh, the propagation pattern for the coarse mesh looks different and reminds of a cup and cone failure mode. These differences can be justified by the fact that the decision of the bifurcation angle in an element is purely based on the numerical determinant value of $\mathbf{Q}$. A better choice may be provided by using the method of Crété et al. (2014) where the angle is chosen which yields the maximum plastic deformation.

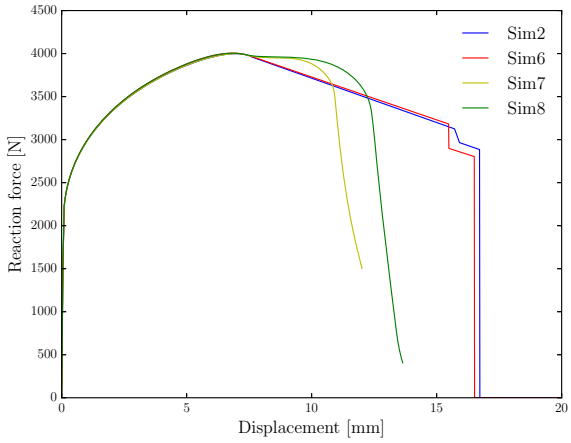

Fig. 16 Evolution of the reaction force for Sim2, Sim6, Sim7 and Sim8, see Table 3 for the nomenclature

4.2.3.3 Comparison of the evolution of the reaction force First of all it is worth analyzing the global response for the case when only the X-FEM, i.e. without incorporating a cohesive law ($t = 0$), in comparison to the case when the X-FEM is combined with a cohesive law. The evolution of the reaction force is shown in Fig. 15. In the case of using only the X-FEM without cohesive law, it can be observed that right at the onset of strain localization the structure is subjected to an abrupt drop in load to zero, i.e. an immediate formation of a crack leading to the total rupture of the structure. If the X-FEM is

combined with a cohesive law, this sudden drop can be retarded and the transition to crack formation takes places in a progressive manner. Then, when the critical rupture traction is reached, the propagation of a macro-crack occurs in the wake of the cohesive band and the load drops to zero almost abruptly.

It should also be paid attention to the fact that a smooth transition from the pre- to the post-localization regime can be achieved—even for the coarse mesh—mainly by computing the internal cohesive force vector from the nodal bulk forces at the onset of localization.

It was already reported that the mesh size influences the direction of propagation. Now, the effect of the mesh size on the global response is examined, see Fig. 16. It can be observed that the pure use of the GTN model leads to severe mesh dependence of the global response. By contrast, the proposed cohesive band propagation method in the context of the X-FEM is nearly insensitive to the mesh size what concerns the global response.

The final Fig. 17 shows the evolution of the reaction forces for different slopes of the cohesive law, which can be well represented for the fine and coarse meshes. Due to the fact that a critical rupture traction has been used, the simulation fails earlier in the case of a larger slope.

5 Concluding remarks

In this chapter a methodology to couple a strain localization induced cohesive band with the X-FEM was proposed and assessed. This approach allows for passing progressively from the phase of void-growth induced damage to crack propagation in ductile materials.

An algorithm was proposed to activate and propagate a cohesive band within the structure until rupture. This model was implemented as a UEL in the commercial FE computation code Abaqus. This methodology was applied to a 2D tensile-loaded plate. It could be shown that using the 4-point Gauss rule for the integration of the bulk part in the enriched elements merely impairs the accuracy of the simulation compared to using an expensive 64-point Gauss rule - even in a coarse mesh. The propagation method has been modified to optimally work with the new integration scheme. The calculation time and storage space can thus be drastically reduced. It was further observed that the propagation path differs between the two simulations. This may be traced back to the mere use of the value of the determinant as decision basis for the propagation angle. In the future, a more sophisticated methodology can be implemented, see e.g. Crété et al. (2014). Regarding the global response, the cohesive law allows passing progressively from diffuse damage to crack propagation and thus avoids the sudden drop in load when only using the standard X-FEM. Then it could be shown that the model behaves nearly mesh independent. Also it could be shown that the transition from diffuse damage to the onset of localization is smooth and without numerical difficulties.

Although some issues still remain to be addressed, the cohesive band methodology in combination with a physics-motivated propagation method has been shown to produce first convincing results. In a prospective work, the parameters of the cohesive law need to be adapted to experimental results for further being used for failure analysis of engineering structures.

Acknowledgements This work has benefitted from the financial supports of DGA/MRIS (French Ministry of Defense) and Région Midi-Pyrénées.

References

Aravas, N.: On the numerical integration of a class of pressure-dependent plasticity models. Int. J. Numer. Methedos Eng. **24**(7), 1395–1416 (1987)

Barenblatt, G.I.: The formation of equilibrium cracks during brittle fracture. General ideas and hypotheses. Axially-symmetric cracks. J. Appl. Math. Mech. USS **23**(3), 622–636 (1959)

Bažant, Z.P., Belytschko, T., Chang, T.P.: Continuum theory for strain-softening. J. Eng. Mech. ASCE **110**(12), 1666–1692 (1984)

Belytschko, T., Black, T.: Elastic crack growth in finite elements with minimal remeshing. Int. J. Numer. Methods Eng. **45**(5), 601–620 (1999)

Belytschko, T., Fish, J., Engelman, B.E.: A finite element with embedded localization zones. Comput. Methods Appl. Mech. **70**, 59–89 (1988)

Belytschko, T., Chen, H., Xu, J., Zi, G.: Dynamic crack propagation based on loss of hyperbolicity and a new discontinuous enrichment. Int. J. Numer. Methods Eng. **58**(12), 1873–1905 (2003)

Camacho, G.T., Ortiz, M.: Computational modelling of impact damage in brittle materials. Int. J. Solids Struct. **33**(20), 2899–2938 (1996)

Camanho, P.P., Dávila, C.G.: Mixed-Mode Decohesion Finite Elements for the Simulation of Delamination in Composite Materials. Tech. rep, NASA/TM-2002-211737, Washington D.C. (2002)

Chu, C.C., Needleman, A.: Void nucleation effects in biaxially stretched sheets. J. Eng. Mater. T ASME **102**(3), 249–256 (1980)

Crété, J.P., Longère, P., Cadou, J.M.: Numerical modelling of crack propagation in ductile materials combining the GTN model and X-FEM. Comput. Method Appl. Mech. **275**, 204–233 (2014)

Dugdale, D.S.: Yielding of steel sheets containing slits. J. Mech. Phys. Solids **8**, 100–108 (1960)

Elguedj, T., Gravouil, A., Combescure, A.: Appropriate extended functions for x-fem simulation of plastic fracture mechanics. Comput. Methods Appl. Mech. **195**(7), 501–515 (2006)

Geuzaine, C., Remacle, J.F.: Gmsh: a 3-d finite element mesh generator with built-in pre- and post-processing facilities. Int. J. Numer. Methods Eng. **79**(11), 1309–1331 (2009)

Gullerud, A.S., Gao, X., Dodds, R.H., Haj-Ali, R.: Simulation of ductile crack growth using computational cells: numerical aspects. Eng. Fract. Mech. **66**(1), 65–92 (2000)

Gurson, A.L.: Continuum theory of ductile rupture by void nucleation and growth: Part i—yield criteria and flow rules for porous ductile media. J. Eng. Mater. T ASME **99**(1), 2–15 (1977)

Haboussa, D., Grégoire, D., Elguedj, T., Maigre, H., Combescure, A.: X-fem analysis of the effects of holes or other cracks on dynamic crack propagations. Int. J. Numer. Methods Eng. **86**(4–5), 618–636 (2011)

Hadamard, J.: Sur les problèmes aux dérivées partielles et leur signification physique. Princet. Univ. Bull. **13**, 49–52 (1902)

Hill, R.: A general theory of uniqueness and stability in elastic-plastic solids. J. Mech. Phys. Solids **6**, 236–249 (1958)

Hillerborg, A., Modéer, M., Petersson, P.E.: Analysis of crack formation and crack growth in concrete by means of fracture mechanics and finite elements. Cem. Concr. Res. **6**, 773–782 (1976)

Huespe, A.E., Needleman, A., Oliver, J., Sanchez, P.J.: A finite thickness band method for ductile fracture analysis. Int. J. Plast. **25**(12), 2349–2365 (2009)

Kanninen, M.F., Popelar, C.L.: Advanced Fracture Mechanics. Oxford University Press, New York (1985)

Krupp, U.: Fatigue Crack Propagation in Metals and Alloys: Microstructural Aspects and Modelling Concepts. Wiley, Hoboken (2007)

Lemaitre, J.: A continuous damage mechanics model for ductile fracture. J. Eng. Mater. T ASME **107**(1), 83–89 (1985)

Li, H., Chandra, N.: Analysis of crack growth and crack-tip plasticity in ductile materials using cohesive zone models. Int. J. Plast. **19**(6), 849–882 (2003)

Longère, P., Dragon, A., Trumel, H., de Resseguier, T., Deprince, X., Petitpas, E.: Modelling adiabatic shear banding via damage mechanics approach. Arch. Mech. **55**, 3–38 (2003)

Longère, P., Geffroy, A.G., Leblé, B., Dragon, A.: Modeling the transition between dense metal and damaged (microporous) metal viscoplasticity. Int. J. Damage Mech. **21**(7), 1020–1063 (2012)

Mandel, J.: Conditions de stabilité et postulat de drucker. In: Sirieys, P., Kravtchenko, J. (eds.) Rhéologie et mécanique des sols. Springer, Berlin (1966)

Moës, N., Dolbow, J., Belytschko, T.: A finite element method for crack growth without remeshing. Int. J. Numer. Methods Eng. **46**, 131–150 (1999)

Needleman, A.: A continuum model for void nucleation by inclusion debonding. J. Appl. Mech. **54**(3), 525–531 (1987)

Oliver, J.: Modeling strong discontinuities in solid mechanics viq strain softening constitutive equations. Part 1: fundamentals. Part 2: numerical simulation. Int. J. Numer. Methods Eng. **39**, 3575–3624 (1996)

Ortiz, M., Leroy, Y., Needleman, A.: A finite element method for localized failure analysis. Comput. Methods Appl. Mech. **61**, 189–214 (1987)

Pijaudier-Cabot, G., Bažant, Z.: Nonlocal damage theory. J. Eng. Mech. ASCE **113**(10), 1512–1533 (1987)

Pourmodheji, R., Mashayekhi, M.: Improvement of the extended finite element method for ductile crack growth. Mater. Sci. Eng. **551**, 255–271 (2012)

Pugno, N., Ciavarella, M., Cornetti, P., Carpinteri, A.: A generalized paris law for fatigue crack growth. J. Mech. Phys. Solids **54**(7), 1333–1349 (2006)

Rousselier, G.: Ductile fracture models and their potential in local approach of fracture. Nucl. Eng. Des. **105**(1), 97–111 (1987)

Siegmund, T., Brocks, W.: A numerical study on the correlation between the work of separation and the dissipation rate in ductile fracture. Eng. Fract. Mech. **67**(2), 139–154 (2000)

Simo, J.C., Hughes, T.J.R.: Computational Inelasticity, vol. 7. Springer, Berlin (2006)

Sukumar, N., Chopp, D.L., Moran, B.: Extended finite element method and fast marching method for three-dimensional fatigue crack propagation. Eng. Fract. Mech. **70**(1), 29–48 (2003)

Thomas, T.Y.: Extended compatibility conditions for the study of surfaces of discontinuity in continuum mechanics. J. Math. Mech. **6**, 311–322 (1957)

Turon, A., Davila, C.G., Camanho, P.P., Costa, J.: An engineering solution for mesh size effects in the simulation of delamination using cohesive zone models. Eng. Fract. Mech. **74**, 1665–1682 (2007)

Tvergaard, V.: Influence of voids on shear band instabilities under plane strain conditions. Int. J. Fract. **17**(4), 389–407 (1981)

Tvergaard, V., Hutchinson, J.W.: The relation between crack growth resistance and fracture process parameters in elastic-plastic solids. J. Mech. Phys. Solids **40**, 1377–1397 (1992)

Wells, G.N., Sluys, L.J.: A new method for modelling cohesive cracks using finite elements. Int. J. Numer. Methods Eng. **50**(12), 2667–2682 (2001)

Westergaard, H.M.: Bearing pressures and cracks. J. Appl. Mech. **61**, A49–53 (1939)

Xu, X.P., Needleman, A.: Numerical simulations of fast crack growth in brittle solids. J. Mech. Phys. Solids **42**(9), 1397–1434 (1994)

Zi, G., Belytschko, T.: New crack-tip elements for xfem and applications to cohesive cracks. Int. J. Numer. Methods Eng. **57**(15), 2221–2240 (2003)